Ionics (2017) 23:3111–3123
DOI 10.1007/s11581-017-2119-5

ORIGINAL PAPER

The order of addition of corn starch/lithium perchlorate/glycerol affects the optical, mechanical, and electrical properties of a solid polymer electrolyte

E.J. Vernon-Carter[1] · J. Alvarez-Ramirez[1] · L.A. Bello-Perez[2] · C. Roldan-Cruz[3] · A. Garcia-Hernandez[1] · L. Huerta[4]

Received: 20 February 2017 / Revised: 3 April 2017 / Accepted: 19 April 2017 / Published online: 27 April 2017

Abstract Optical, mechanical, and electric properties of solid polymer electrolyte (SPE) were affected by the order of addition of corn starch (S), lithium perchlorate (Li), and glycerol (G) during the preparation process. Four formulations were made based on whether Li was added prior to S gelatinization (simultaneous formulations SGLi and SLi+G) or whether it was added after S was gelatinized (sequential formulations SG+Li and S+LiG). Simultaneous formulations produced films with smaller elongation-at-break response (60–75%) relative to their sequential counterparts (75–82%). The simultaneous formulations exhibited higher electrical conductivity (~0.7 mS cm^{-1}) and capacitance (~0.017 F cm^{-2}) and electrochemical stability than the sequential formulations (~0.9 mS cm^{-1} and ~0.012 F cm^{-2}) at room temperature. Results from FTIR and DSC analyses indicated that starch re-crystallization in casting phase could lead to variations on electrical properties for the different SPE formulations. It was postulated that Li cations replace hydrogen ions inside starch molecules, retarding the re-crystallization of starch molecules.

Keywords Solid polymer electrolyte · Corn starch · Lithium perchlorate · Order of addition · Re-crystallization

✉ J. Alvarez-Ramirez
jjar@xanum.uam.mx

[1] Departamento de Ingeniería de Procesos e Hidráulica, Universidad Autónoma Metropolitana-Iztapalapa, Apartado Postal 55-534, 09340 Ciudad de México, Mexico

[2] Centro de Desarrollo de Productos Bioticos, Instituto Politécnico Nacional, Km 6 Carr. Yautepec-Jojutla, Calle Ceprobi No. 8, Colonia San Isidro, Apartado Postal 24, 62731 Yautepec, Morelos, Mexico

[3] Departamento Biotecnología, Universidad Autónoma Metropolitana-Iztapalapa, Apartado Postal 55-534, 09340 Ciudad de México, Mexico

[4] Instituto de Investigación en Materials, Universidad Nacional Autónoma de México, 04500 Ciudad de México, Mexico

Introduction

In the recent decade, solid polymer electrolytes (SPE) have been increasingly considered for a diversity of applications as these materials can achieve similar electrical performance as their liquid counterparts. Besides, safer handling, mechanical robustness, and compact cell assemblage are advantages offered by SPE over liquid electrolytes. In the earlier stages of SPE development, synthetic polymers were considered as host material, including polyethylene oxide [1], polyacrylic acid [2], and polyvinyl alcohol [3], with promising results. The techniques for polymer synthesis offered a rich spectrum for fabricating complex blends of polymeric materials. However, the use of synthetic polymers was confronted to environmental shortcomings linked to their toxicity and slow degradability. In this regard, research efforts moved to the search of environmentally friendly materials with properties capable to deliver adequate mechanical and electrical requirements. Thus, biopolymers were immediately considered as an alternative to synthetic polymers as they are both safe and environmentally friendly. Starch [4], chitosan [5], cellulose [6], xanthan gum [7], and gelatin [8] are commercially available biopolymers that have been explored for SPE purposes. The production of these natural polymers is sustainable and they are biodegradable by standard methods (e.g., aerobic sludge and soil consortiums).

Starch is highly abundant, relatively inexpensive, and botanically diverse, with molecular structure composed by

repeating 1,4-α-D-glucopyranosyl units leading to linear amylose chains and branched and amylopectin chains [9]. Depending on the botanical source, starch generally contains 20 to 25% amylose and 75 to 80% amylopectin by weight. Although native starch granules exhibit a semicrystalline structure [9], its aqueous dispersions can be easily gelatinized to obtain films with highly amorphous microstructure. Indeed, amorphous microstructure is desired to achieve high electrical (e.g., conductivity and capacitance) performance under ionic transport mechanisms. First studies on the issue found that acceptable high conductivity due to non-Debye behavior was obtained with starch/ammonium nitrate system [4]. It was reported that amylopectin-rich starch plasticized with glycerol showed conduction stability over 6 months [10]. Blends of chitosan and starch with glycerol as plasticizer exhibited good performance for electrical supercapacitance [11, 12]. Potato starch/ammonium oxide films performed well over a wide range of frequencies [13]. Recently, the potential of starch-based SPE for energy power applications under safety, low-cost, and high sustainability requirements was exposed [14].

The typical formulation of starch-based SPE involves aqueous starch dispersion (2–3% *w*/*w*), a Li salt acting as doping cation and a plasticizer (e.g., glycerol) to stabilize the electrolyte microstructure. Starch is a semicrystalline powder that under heating in excess water undergoes swelling and dissolution. During the heating process, starch granules are partially dissolved due to swelling-leaching of amylose molecules and small amounts of amylopectin into the aqueous phase [15, 16]. Some authors have used a simultaneous approach for fabricating the solid polymer electrolytes, which basically consists in mixing starch, salt, and plasticizer in distilled water and heating at about 75–90 °C under gently stirring conditions [14, 17, 18], while others have favored a sequential procedure where starch is firstly gelatinized and then added with glycerol and Li salt [10, 19]. However, the effect of the order of addition of the SPE components (starch, Li salt, and plasticizer) on the optical, mechanical, and electrical properties is an issue that has not been addressed. The addition order is an important issue since the gelatinized dispersion can undergo re-crystallization of starch chains [20] during the casting process, which could limit the electrical performance of the solid electrolyte as the mobility of ions is favored by amorphous structures [19–21]. In this respect, it is not clear how the addition order of the SPE components affects the re-crystallization process and hence the electrical performance of the casted electrolytic film.

The aim of this work was to study the effect of the order of addition of corn starch, lithium perchlorate, and glycerol on the optical, mechanical, and electrical properties of starch-based solid polymer electrolytes.

Materials and methods

Materials

Corn starch (S; CAS number 9005-25-8, amylose content 25.3% *w*/*w*, moisture content <15%, pH 4.8, ash <0.5%, protein <0.1%), lithium perchlorate (Li; $LiClO_4$, CAS number 7791-03-9, purity >99.99%), and glycerol (G; $HOCH_2CH(OH)CH_2OH$, CAS number 56–81-5, purity ≥99.5%) were purchased from Sigma-Aldrich (Toluca, Mexico). Starch was dried under inert atmosphere at 55 °C for 24 h before use. All experiments were conducted with deionized water (electrical resistivity ~32.6 MΩ cm).

Solid polymer electrolyte film preparation

To assess the effect of the order of addition of S, Li, and G on the optical, mechanical, and electrical properties of the SPE, four formulations were considered. The order of addition of Li plays an important role in the final properties of the SPE. In this way, two simultaneous and two sequential formulations were designed. In the former cases, Li was incorporated to S before the gelatinization process. In the latter cases, Li was added after S was gelatinized. In this respect, the simultaneous formulations can be described as follows:

1. *Formulation SGLi*: S (40.0 g), G (20.0 g), and Li (6.0 g) were dispersed in water (1 L), gently stirred with a mechanical mixer (250 rpm for 5 min), and heated at 90 °C during 30 min with constant stirring (250 rpm) in a water bath shaker.
2. *Formulation SLi+G*: S (40.0 g) and Li (6.0 g) were dispersed in water (1 L), gently stirred with a mechanical mixer (250 rpm for 5 min), and heated at 90 °C during 30 min with constant stirring (250 rpm) in a water bath shaker. Then, G (20.0 g) was added to the dispersion at room temperature and stirred for 1 h.

On the other hand, the sequential formulations can be described as follows:

3. *Formulation SG+Li*: S (40.0 g) and G (20.0 g) were dispersed in water (1 L), gently stirred with a mechanical mixer (250 rpm for 5 min), and heated at 90 °C during 30 min with constant stirring (250 rpm) in a water bath shaker. Afterwards, Li (6.0 g) was added to the dispersion at room temperature and stirred for 1 h.
4. *Formulation S+LiG*: S (40.0 g) was dispersed in water (1 L), gently stirred with a mechanical mixer (250 rpm for 5 min), and heated at 90 °C during 30 min with constant stirring (250 rpm) in a water bath shaker. Subsequently, Li (6.0 g) and G (20.0 g) were added to the dispersion at room temperature and stirred for 1 h.

To prepare the films, 5 mL of the viscous film-forming dispersions was casted onto a Teflon plate and left to dry for 48 h at 40 °C. All the films reached equilibrium moisture content (determined gravimetrically) within 1 week of storage in the desiccators.

Other formulations are possible. For instance, the formulation S+Li+G involves the gelatinization of starch in the first step and the subsequent addition of the Li salt. The plasticizer is incorporated in a third step. The results of this formulation were similar to the results obtained for the S+LiG formulation. However, the results revealed that the order of addition of the Li salt is the main factor determining the mechanical and electrical properties of the film. In this way, to focus on the main mechanisms involved in the film properties as induced by order effects, we only studied in detail the four formulations described above.

Film characterization

Scanning electron microscopy (SEM) was performed on the film samples to explore surface microstructure features. Samples were coated with a thin layer of gold in a Fine Coat Ion Sputter JFC 1100 (JEOL Ltd., Akishima, Japan). A high vacuum JEOL Scanning Electron Microscope JMS-6360LY (JEOL Ltd., Akishima, Japan), at 20 kV, was used to record each sample at magnification of ×2000. Representative SEM micrographs were presented to illustrate the surface features.

Film opacity was measured with a UV-Visible Spectrophotometer (Spectronic Genesys 2, Thermo Electron Corporation, Madison, WI, USA) and is defined as the area under the absorbance spectrum between 400 and 800 nm according to ASTM D 1003-00 method [22]. Film thickness was estimated with a micrometer caliper (1 μm accuracy, Mitutoyo Manufacturing Co. Ltd. Kawasaki, Japan). Thickness measurements were conducted at room temperature (20 °C) and repeated on ten random positions of each film specimen. The contact angle between the film and water was determined with the optical contact angle device OCA 20 (Dataphysics Instruments GmbH, Filderstadt, Germany) at 25 °C. Tensile strength (MPa) and elongation at break (%) were evaluated in a tensile test using a texture analyzer CT3 (Brookfield AMETEK, Middleboro, MA, USA) with a dual grip assembly following the standard ASTM D882-00 method [23]. For testing, the films were cut into strips (1 × 10 cm) and conditioned at 50% RH for about 48 h. The force and the distance were measured during extension of the strips at 60 mm/min up to break. Initial grip separation and mechanical crosshead speed were set at 30 mm and 1 mm s^{-1}, respectively. The tensile strength was estimated by dividing the maximum load by cross-sectional area of the film (thickness × width), while the elongation at break was obtained as the percentage of extension at the moment of rupture.

XRD spectra were measured at room temperature with a Siemens D-5000 diffractometer (Karlsruhe, Germany) using Cu-Kα radiation (k = 1.543), and a secondary beam graphite monochromator was operated at 40 kV and 30 mA. Intensities were measured in the 5–50° range with a 0.03° step size and measuring time of 2.0 s per point. Diffractograms were smoothed (Savitsky-Golay, polynome = 2, points = 15) and baseline-corrected by drawing a straight line at an angle of 7°. The relative crystallinity was measured according to the Hermans-Weidinger method [24, 25]. In a first step, the XRD curve is deflated by a XRD spectrum of fully amorphous starch obtained by the repeated application of heat moisture treatment and drying. The relative crystallinity was estimated as the area produced by the deflated XRD spectrum.

Fourier transform infrared (FTIR) spectra of the films were obtained by means of a PerkinElmer spectrophotometer (Spectrum 100, PerkinElmer, Waltham, MA, USA) equipped with a crystal diamond universal ATR sampling accessory and mirror velocity of 0.4 cm s^{-1}. During measurements, the sample was in contact with the universal diamond ATR top plate. A spectrum of the empty cell was used for correcting by background effects. For each sample, the spectrum represented an average of three scans with resolution of 1 cm^{-1}. Also, spectra were baseline-corrected at 1200–900 cm^{-1} by drawing a straight line below the recorded signal. In this case, the assumed line shape was Lorentzian with a half-width of 15 cm^{-1}. A half-width of 22 cm^{-1} and a resolution enhancement factor of 2.2 were used. The measurements were conducted at room temperature.

X-ray photoelectron spectroscopy (XPS, K-ALPHA, Thermo Scientific, Waltham, MA, USA) measurements were carried out as follows. All spectra were collected using Al-Kα radiation (1486.6 eV), monochromatized by a twin crystal monochromator, yielding a focused X-ray spot with a diameter of 400 μm, at 3 mA × 12 kV. The alpha hemispherical analyzer was operated in the constant energy mode with survey scan pass energies of 200 eV to measure the whole energy band.

Electrochemical impedance spectroscopy (EIS) measurements were carried out using a HIOKI 3532-50 LCR HiTester (Hioki E.E. Corporation, Nagano, Japan) in the frequency range from 1 Hz to 50 MHz at room temperature. To this end, the electrolytes were placed between two carbon blocking disc electrodes under the pressure of two springs. The bulk resistance (R_b) was estimated from Nyquist plots of the EIS measurements. The conductivity (σ) was obtained from the following equation:

$$\sigma = \frac{d}{R_b A} \tag{1}$$

where A is the contact area (~1.0 cm^2) and d is the thickness of the electrolyte film (~0.1–0.2 mm). On the other hand, cyclic

voltammetry (CV) was performed using PARSTAT Potentiostat/Galvanostat 2273 (Princeton Applied Research, Oak Ridge, TN, USA). CV tests were carried out at scan rate 10 mV s^{-1} between 0.0 and 1.0 V using a two-electrode configuration.

Statistical analyses

Data were analyzed using a one-way analysis of variance (ANOVA) and a Tukey's test for a statistical significance $P \leq 0.05$, using the SPSS Statistics 19.0. All experiments were done in triplicate.

Results

Surface morphology

Figure 1 presents illustrative images of the surface of the four films. Porous structures were observed for simultaneous formulations (SGLi and SLi+G), while smooth surfaces were exhibited by sequential formulations (SG+Li and S+LiG). This suggests that the gelatinization of the starch dispersion under the presence of the Li ions led to fracture formation, an effect that could be caused by the formation of weaker gels. In all films, the presence of insoluble remnants distributed on the film surface can be observed. These structures are highly elastic, conferring mechanical stability and protection in the face of water molecules [26].

Opacity and mechanical response

The thickness, opacity, and mechanical properties of the SPE films are given in Table 1. The film thickness varied in the range 29–32 μm, regardless of the order of addition. The second column of Table 1 presents the values of the opacity for the different SPE formulations. The formulation SG+Li displayed the highest opacity value (~161.02 a.u.), followed by formulation SGLi, while the formulation S+GLi presented the lowest opacity value (~111.27 a.u.). The differences of opacity might be attributed to subtle differences in starch chain/glycerol interactions as affected by the addition order. When starch was gelatinized in the presence of glycerol, the plasticizer was able to achieve a more extensive covering of the starch chains, than when added after starch gelatinization. In turn, this effect could be leading to higher opacity values.

The order of addition also affected the mechanical response of the different SPE films. The formulation SLi+G presented the lowest elongation-at-break value (~60.05%), while the formulation SG+Li displayed the highest value. The heating of the plasticizing agent simultaneously with the starch chains produced films with improved mechanical response, an effect that was already observed for non-conductive films made with starch and montmorillonite [27]. In contrast, the sole addition

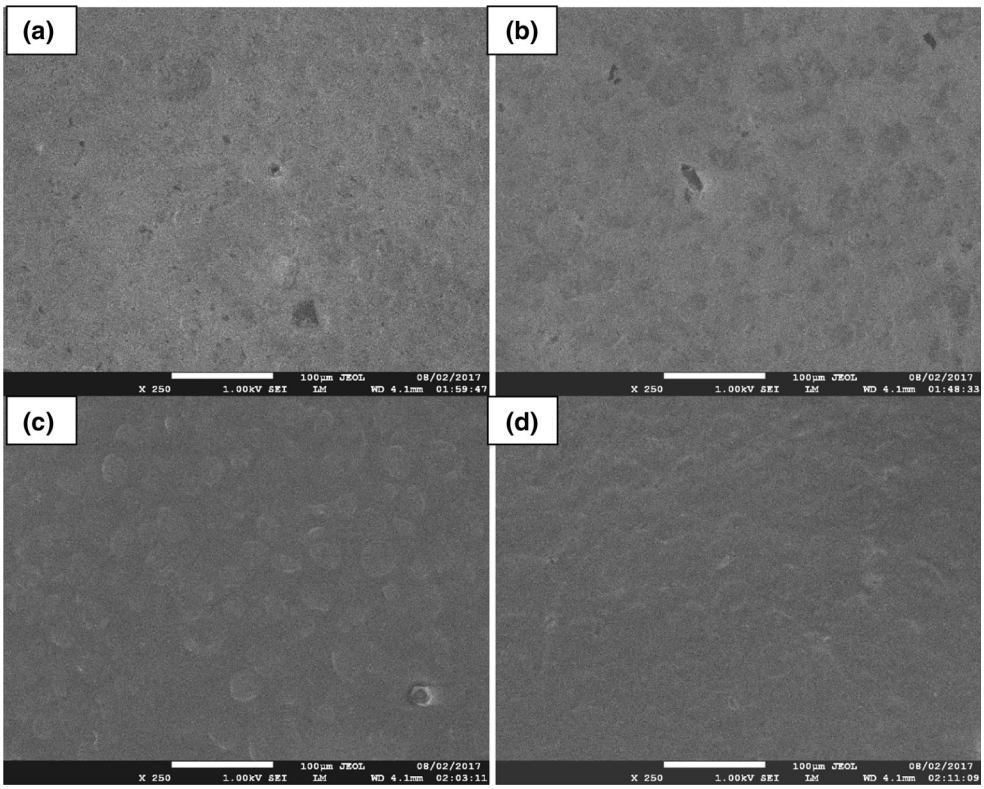

Fig. 1 SEM images of film surfaces. **a** SGLi. **b** SLi+G. **c** SG+Li.**d** S+LiG

Table 1 Thickness, opacity, and mechanical properties of corn starch films

Film code	Thickness (μm)	Opacity (a.u.)	Elongation-at-break (%)	Tensile stress (MPa)	Young's modulus
SGLi	29.2 ± 0.1[a]	137.66 ± 1.56[b]	75.42 ± 1.2[b]	1.03 ± 0.07[a]	1.36 ± 0.05[a]
SLi+G	30.6 ± 0.2[a]	114.42 ± 2.02[c]	60.05 ± 1.5[c]	0.86 ± 0.06[c]	1.44 ± 0.07[b]
SG+Li	29.8 ± 0.2[a]	161.02 ± 2.13[a]	82.65 ± 1.3[a]	0.91 ± 0.06[b]	1.15 ± 0.05[c]
S+GLi	30.2 ± 0.1[a]	111.27 ± .96[cd]	75.23 ± 1.1[b]	0.85 ± 0.05[c,d]	1.13 ± 0.06[c]

Values are means ± standard error, of three replicates. Superscripts with different letters in same column indicate significant differences ($P \leq 0.05$).

of the Li salt during the gelatinization process led to the most fragile films. In fact, the formulation SLi+G presented the highest stiffness value as indicated by the Young's modulus in the last column of Table 1. Oosten [28] found that metallic cations penetrate and stabilize the structure of starch granules. However, the anions (like CLO_4^-) promote the starch dissolution by rupturing hydrogen bonds. In turn, this effect produced weak starch hydrogels. Similar effects were observed for alkali treatment of starch granules [29]. Summing up, it seems that the simultaneous addition of Li to S has a detrimental effect in the mechanical response of the SPE films.

X-ray analysis

Linear amylose and branched amylopectin chains are the main molecular components of starch granules. These chains are arranged within a complex structure formed by alternating crystalline/amorphous rings organized around the central hilum. Corn starch granules display A-type crystallinity, which is characterized by intensity bands at about 15.0°, 17.0°, 18.0°, and 23.0° in the X-ray diffraction pattern. During heating, water is absorbed in the amorphous regions of granules, leading to swelling and subsequent gelatinization. Water intrusion provokes the disruption of tightly bound areas of double-helix structures of amylopectin, which eventually destruct the internal microstructure. During the gelatinization process, amylose chains are released, viscosity is increased, and randomness is increased [16]. Figure 2a presents the X-ray diffraction pattern of films for the four SPE film formulations. A broad intensity band at about 20.2° was observed for all cases, reflecting the incipient crystallinity of insoluble, amylopectin-rich insoluble remnants [30, 31]. This pattern is characteristic of starch-based SPE [32, 33], indicating that the film microstructure is highly amorphous. Indeed, amorphous microstructure is desired to achieve high electrical (e.g., conductivity and capacitance) performance under ionic transport mechanisms. The SGLi formulation where the three components are added simultaneously displayed small intensity peaks at about 17.1° and 22.0°, which are related to the corresponding intensity peaks of native corn starch. In turn, this suggests that the gelatinization of starch granules was incomplete when Li and G were simultaneously added to S. The relatively crystallinity, estimated according to the Hermans-Weidinger method [24, 25, 34], is displayed in Fig. 2b. The estimated relative crystallinity was too low (not higher than 5%) for all SPE formulations, with the higher value for the formulation SGLi. This is an expected result since the patterns of X-ray diffraction shown in Fig. 2a are characteristic of amorphous materials.

FTIR analysis

The XRD results in Fig. 2a showed that the crystallinity of the native starch granules was practically destroyed by the effect of heating under excess water conditions. However, gelatinized starch gels are thermodynamically unstable in the sense that starch chains tend to regroup into new structures. The process is known as gel retrogradation and involves linear amylose chains, and linear parts of branched amylopectin

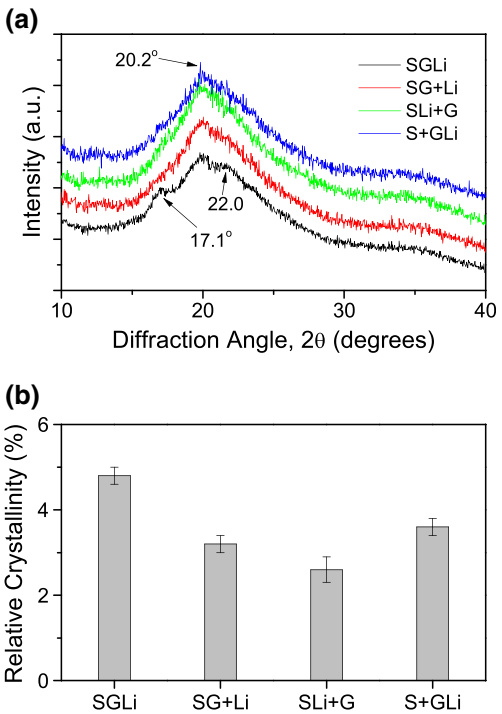

Fig. 2 **a** X-ray diffraction pattern of films for the four SPE film formulations. **b** Relative crystallinity estimated from the XRD patterns described above

molecules arranging themselves into short-size crystalline structures dispersed in the aqueous gel [16, 35]. Recrystallization takes place during drying of the casted dispersion and can be completed within the first 6–10 h of the process. The large amount of amorphous material dispersed in the film induces strong background noise in XRD measurements (Fig. 2a), which hampers the detection of the crystalline structures resulting from the retrogradation process. Instead, FTIR analysis is commonly considered to evaluate the extent of retrogradation. Figure 3a presents the FTIR pattern for the four SPE formulations in the range from 3000 to 950 cm^{-1}. The wide intensity band at about 3600–3000 cm^{-1} is related to OH stretching and the peak at 2930 cm^{-1} to C–H stretching. It can be appreciated that the addition order had only slight effects on the intensity and shape of these FTIR bands. In contrast, the behavior of the FTIR spectra in the region from 1100 and 950 cm^{-1} showed important variations with SPE formulation. This FTIR region has been linked to C–O–C interactions and has been shown to be sensitive to changes in molecular arrangement within the short-range order [36]. In fact, short-range order reflects double helical order as opposed to long-range order related to the complex packing of double helices. The band at about 1048 cm^{-1} is sensitive to crystallinity content, while the band at about 1020 cm^{-1} has been related to vibration of amorphous components. On the other hand, the band at about 995 cm^{-1} is sensitive to hydrated crystalline domains [37]. It is noted that the band at about 1048 cm^{-1} was hardly sensitive to the addition order. However, the relative intensity of the other two bands was quite sensitive to SPE film formulation. In this regard, one can consider the ratio $R_{995/1020}$ as an index of the short-range crystallinity of the film. However, the absorbance bands of FTIR spectra are commonly affected by overlapping effects, such that the read out of the absorbance value might be quite inaccurate. To avoid this situation, deconvolution of the FTIR spectrum is carried out by means of, e.g., Gaussian basis functions. To this end, the spectrum was baseline-corrected by drawing a straight line and deconvoluted with Gaussian basis functions with a half-width of 15 cm^{-1} and resolution enhancement factor of 1.5. Figure 3b illustrates the deconvoluted spectrum with three Gaussian functions. The peaks of the basic functions were located at 1047, 1020, and 994 cm^{-1} and were shifted from the nominal values reported in the literature. The shift was likely induced by the presence of the Li cation, which interacts with the starch chains [38]. In this way, the index $R_{995/1020}$ will be considered as the ratio of the areas for the Gaussian curves with peak values close to the wave numbers 1020 and 995 cm^{-1}. Figure 3c presents the results of the index $R_{995/1020}$ for the four SPE film formulations. The smallest value (~0.91) was exhibited by the formulation SLi+G, while the maximum value (~1.16) by the formulation S+GLi. These results suggest that the order of addition of the film components had an important effect on starch chain retrogradation during the casting process.

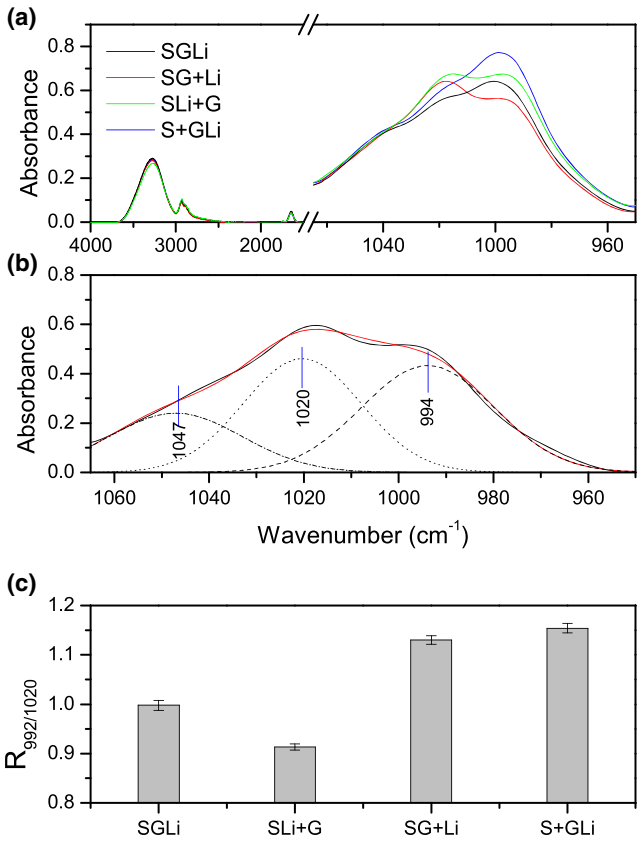

Fig. 3 **a** FTIR pattern for the four SPE formulations in the range from 3000 to 950 cm^{-1}. **b** Example of deconvoluted spectrum with three Gaussian functions. **c** Short-range crystallinity index $R_{995/1020}$ for the four SPE film formulations

DSC analysis

DSC analysis is also a useful tool to gain insights regarding the ordering of the starch-based electrolytic films. The idea behind the DSC analysis is that ordered structures, including retrograded crystalline structures, require energy to disorder (e.g., melt) when subjected to heating. Figure 4a presents the endothermic heat flow traces for the four SPE film formulations in the range from −40 to 200 °C. All the SPE film formulations showed a small endothermic peak located at about −31.0 °C, which could reflect desorption of residual free water molecules in the starch-glycerol matrix [39]. A prominent band was located in the range 79–91 °C, which reflects the melting of short-range crystalline structures (e.g., double-helix aggregates) formed during the retrogradation process. This endothermic band reflects the transition from a glass-like phase to a rubbery (i.e., viscoelastic) solid. In this way, the onset temperature can be taken as an estimate of the glass transition temperature of the starch film [40]. The estimate glass transition temperature ranged from about 27 °C for the formulation SGLi to about 35 °C for the formulation SLi+G,

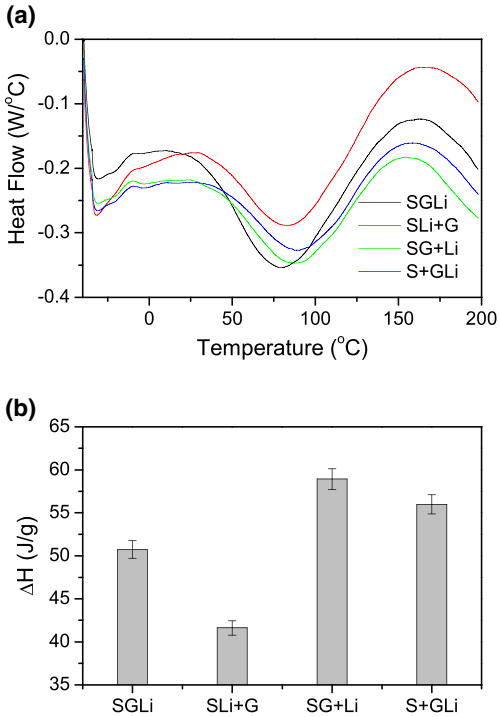

Fig. 4 **a** Endothermic heat flow traces for the four SPE film formulations in the range from −40 to 200 °C. **b** Total endothermic heat obtained by integrating the DSC curve over the scrutinized temperature range

and these values are in line with previous reports for starch-based films with low moisture levels [41]. Figure 4b presents the total endothermic heat obtained by integrating the DSC curve over the scrutinized temperature range. This enthalpy reflects the extent of the ordered structures contained in the film. The formulation SLi+G presented the smallest value (~41.61 J g^{-1}), indicating that this film was the more amorphous one. On the other hand, the formulation SG+Li presented the highest value (~58.92 J g^{-1}), suggesting that this film contained the more ordered structures. Interestingly, these results are in agreement with the FTIR results (Fig. 3c) where the formulation SLi+G presented the smallest value of the ratio $R_{995/1020}$.

XPS analysis

The XPS analysis of the samples revealed the expected result that carbon and oxygen are the major elements, which are reflected in the energy bands 292–280 eV (Fig. 5a) and 538–528 eV (Fig. 5b), respectively. Differences in the XPS patterns can be observed, suggesting that the addition order impacted the configuration of carbon and oxygen in the film structure. To unhide the relative contribution of the different carbon and oxygen bonds, the XRD patterns were deconvoluted with Gaussian basis functions and least-squares numerical adjustments. Figure 5c, d illustrates typical

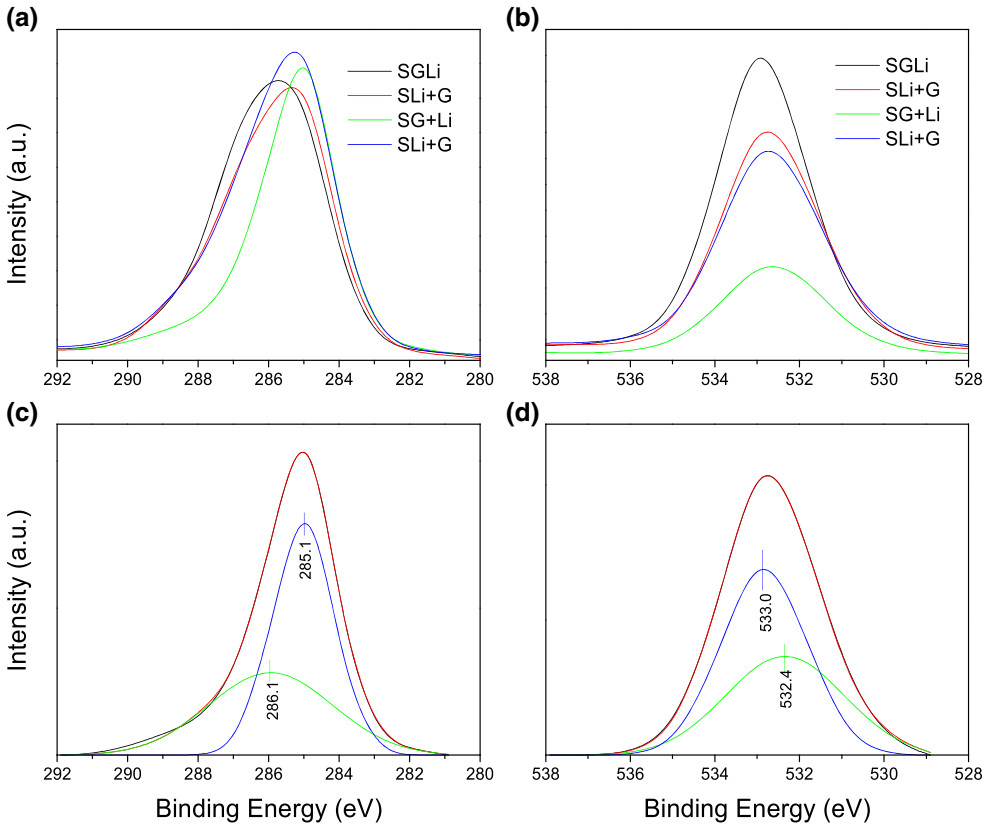

Fig. 5 **a** Carbon and **b** oxygen XPS bands for the different film formulations. Panels **c** and **d** illustrate the deconvolution of the XPS spectra by means of Gaussian basis functions

deconvolution results, showing that two Gaussian functions suffice to describe accurately the curves. For the carbon band, the peaks are located at about 285.0 and 286.2 eV. The former peak can be attributed to carbon atoms bonded only with carbon or hydrogen atoms (e.g., C–C and C–H) and the second peak to carbon atoms bonded with one oxygen atom (e.g., C–O) [42]. The relative contribution of the two peaks was quantified by the ratio $R_{285/286.5}$, and the results are summarized in the first column of Table 2. The ratio exhibits important differences reflecting the effect of the addition order of the film components. On the other hand, the oxygen band has two peaks at about 532.2 and 532.8 eV. The first peak can be attributed to carbonyl (e.g., C=C and O–C=O) groups while the second peak to alcohols and ethers (e.g., C–O–H, C–O–C). The presence of the alcohol group was expected since glycerol belongs to alcohol compounds. Similarly, the ratio $R_{532.2/532.8}$ denotes the contribution of carboxyl groups relative to alcohol groups, and the results are summarized in the second column of Table 2.

Impedance analysis

Figure 6a presents a log-log Nyquist plot of the four SPE film formulations. The Nyquist plot is composed by a small semicircle for high frequencies and a tilted spike for low frequencies. It has been postulated that the semicircle curve can be attributed to ionic conduction in the bulk of the electrolyte [43], which presumably is induced by the parallel combination of bulk resistance and bulk capacitance of polymer electrolytes [44]. In contrast, the tilted spike has been linked to electrode polarization, which is a distinctive feature of diffusion processes [45]. The tilted spike describes anomalous diffusion transport across the film bulk. This effect is commonly described by a constant-phase element with exponent α. Figure 6b presents the estimated values of the CPE exponent, with the SLi+G formulation having the highest value. The values of R_b were determined from the intercept of the semicircle curve with the real axis of the low frequency circle, and the results are presented in Fig. 6c. In line with the conductivity results, the lower bulk resistance from impedance analysis was presented by the film with the highest conductivity. It can

Table 2 Relative contributions of carbon and oxygen in the XPS bands

Film code	$R_{285/286.5}$	$R_{532.2/532.8}$
SGLi	1.12 ± 0.02^{b}	0.65 ± 0.01^{c}
SLi+G	0.33 ± 0.01^{d}	1.38 ± 0.02^{a}
SG+Li	1.45 ± 0.03^{a}	0.53 ± 0.02^{d}
S+GLi	0.78 ± 0.02^{c}	1.11 ± 0.01^{b}

Values are means ± standard error, of three replicates. Superscripts with different letters in same column indicate significant differences ($P \leq 0.05$).

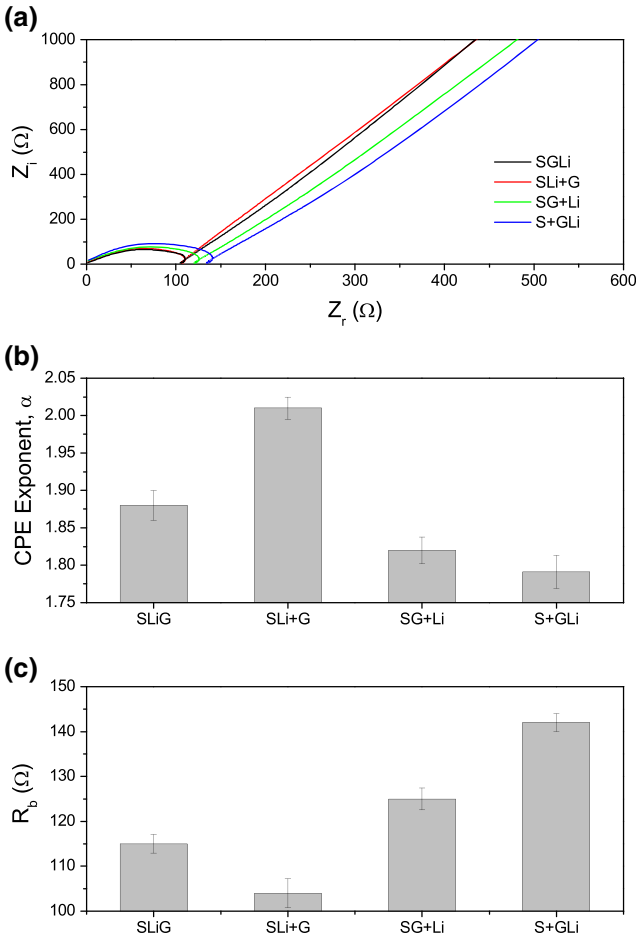

Fig. 6 **a** Log-log Nyquist plot of the four SPE film formulations. **b** Exponent of the tilted spike. **c** Bulk resistance R_b determined from the intercept of the semicircle curve with the real axis of the low frequency circle

be observed that the inclination of the tilted spike was less than 90°, an effect that has been related to inhomogeneous distribution of the added salt in the film matrix or simply to roughness of the electrolyte-electrode interface [46]. The highest inclination (~83°) was displayed by the formulation SLi+G, while the smallest inclination (~76°) was presented by the formulation S+GLi. If one accepts that inhomogeneous distribution of the added Li salt is behind the deviations of the tilt angle from the value of 90°, then the above result is in line with conductivity results to be shown later. In other words, the simultaneous formulations where S added with Li dispersions were gelatinized led to a more homogeneous distribution of Li cation in the starch chain microstructure.

Conductivity analysis

Figure 7a presents the conductivity as function of temperature for the four SPE film formulations. The results are in line with reported values of electrical conductivity for starch-Li films. In fact, corn starch doped with lithium acetate exhibited

electrical conductivity of the order of 0.01–0.02 mS cm^{-1} [47]. Corn starch added with 40% *w/w* lithium perchlorate presented values of the order of 0.01–0.05 mS cm^{-1} [48]. At room temperature (20 °C), the formulation SLi+G exhibited the highest conductivity (~0.93 mS cm^{-1}) and the formulation SG+Li the lowest one (~0.70 mS cm^{-1}). However, some changes were observed as the temperature was increased. For instance, the conductivity of the formulations SGLi and SLi+G was similar for temperatures higher than 40 °C. Similar behavior was obtained for the formulations SG+Li and S+GLi. This suggests that the main determinant of film conductivity is the order of addition of the Li salt, rather than the plasticizer. On the other hand, the increase of the conductivity with temperature can be attributed to two effects: the increase of mobility of the Li cation and to partial melting of retrograded starch chains obtained during the casting process. Evidence of the latter effect can be observed in the endothermic heat flow traces exhibited in Fig. 4a where the onset temperature of the broad band related to melting of short-range (e.g., double-helix) ordered structures was about 25–40 °C. The melting of such structures increases the amorphous regions of the film and hence increases the hopping mechanisms between coordinating sites [47]. Figure 7b presents plot log(σ) versus 1/T for the data in Fig. 7a. The linear variation of this plot indicates that the conductivity followed an Arrhenius-type thermal activated process according with the following expression:

$$\sigma = \sigma_0 \exp\left(-\frac{E_A}{kT}\right) \tag{2}$$

where E_A is the activation energy and $k = 8.617 \times 10^{-5}$ eV K^{-1} is the Boltzmann constant. The activation energy is shown in Fig. 7c. The highest conducting electrolyte presented the lowest activation energy, which is in agreement with the short-range ordering results presented in Fig. 3b, c. The energy barrier for the cation transport decreased with the increase of amorphous structures in the conducting film.

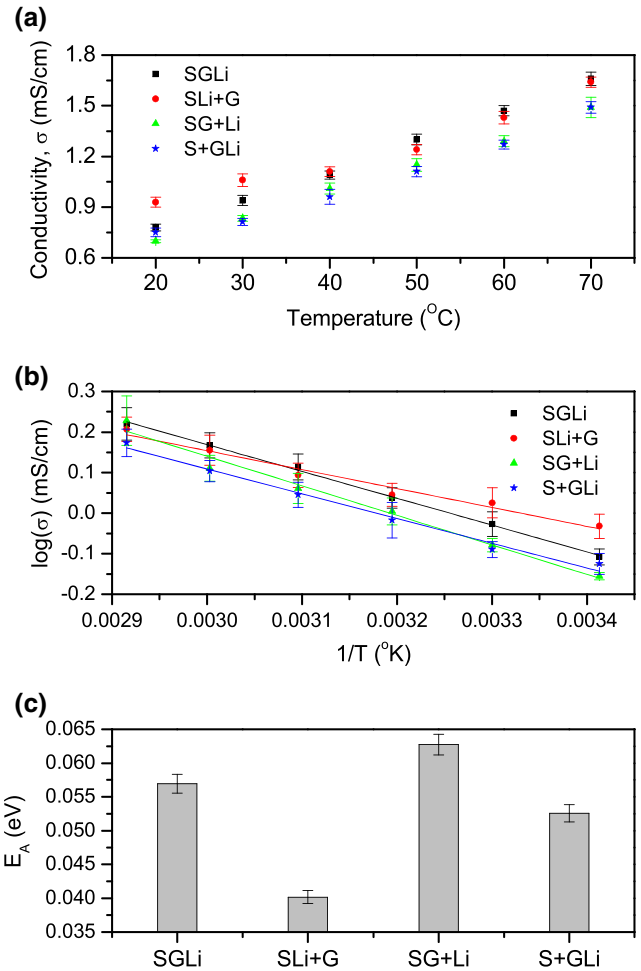

Fig. 7 **a** Electrical conductivity as function of temperature for the four SPE film formulations. **b** Plot log(σ) versus 1/T for the electrical conductivity data. **c** Activation energy for the four SPE film formulations

Cyclic voltammetry analysis

Cyclic voltammetry runs were carried out for assessing the double-layer capacitance of the SPE film formulations. The experiments were carried out at a scan rate of 10 mV s^{-1} for potentials from 0.0 to 1.0 V, starting on the anodic direction. The resulting voltamperograms for the fresh SPE film formulations are displayed in Fig. 8a, for which clear redox peaks are not observed. The rectangular-like pattern of the cyclic voltammetry response is a distinctive feature of double-layer capacitance where charge-discharge processes are taking place in either anodic and cathodic directions. The double-layer capacitance can be estimated by integration of the current-potential response according to the following equation:

$$C_E = \frac{\int_{E_{min}}^{V_{max}} I(V)dV}{\upsilon(V_{max} - V_{min})} \tag{3}$$

where υ is the scanning rate and V_{min} and V_{max} are the minimum and maximum voltages, respectively. Figure 8b presents the estimated capacitance value for the four SPE formulations. The highest value of capacitance (~0.18 F cm^{-2}) was presented by the formulation SLi+G and the lowest value (~0.13 F cm^{-2}) by the formulation S+GLi. In general, the simultaneous formulations (where Li was added to starch before gelatinization) presented higher capacitance levels than the sequential formulations (where the Li was added after starch gelatinization). This suggests that the proper bonding of the Li cation into the starch microstructure plays a central role in the performance of the starch-based electrolyte.

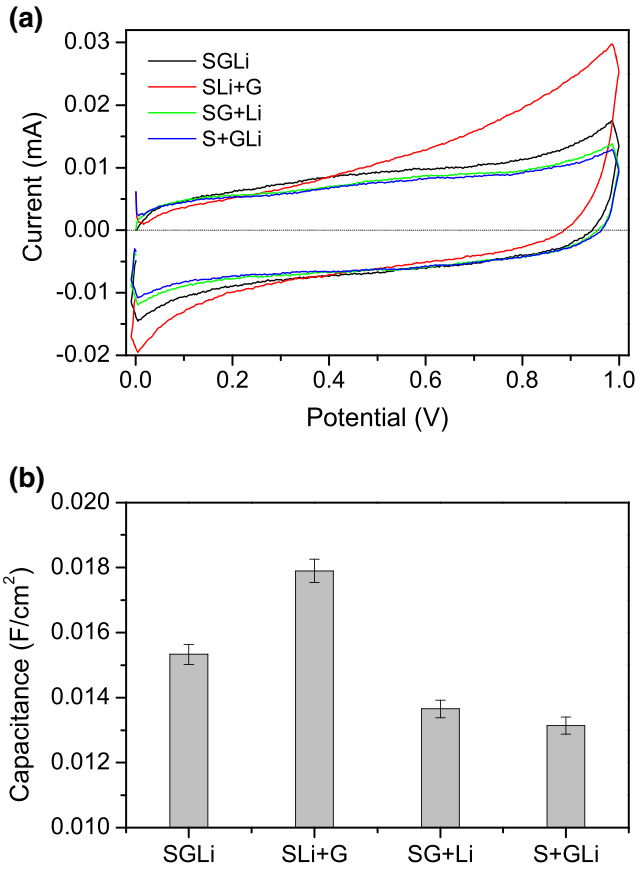

Fig. 8 **a** Voltamperograms for the fresh SPE film formulations. **b** Estimated capacitance value for the four SPE formulations

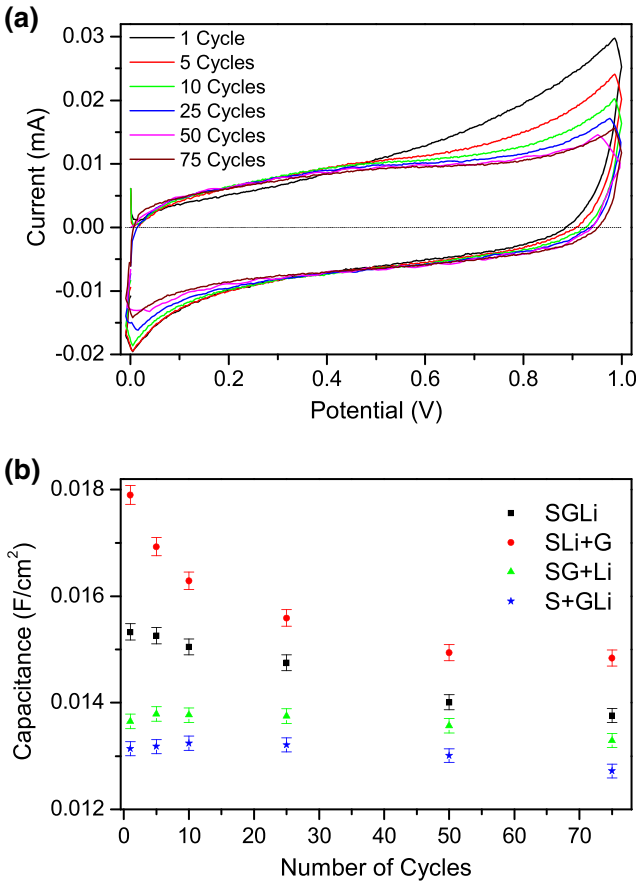

Fig. 9 **a** Current/potential response for different number of potential cycles. **b** Capacitance as function of the number of cycles

To test the electrochemical stability, the SPE film formulations were subjected to repeated voltammetry cycles. The underlying idea is that the SPE film can undergo irreversible oxidation/reduction reactions when subjected to multiple charge/discharge cycles. Figure 9a illustrates the current/potential response for different number of potential cycles. It is noticeable that the anodic current decreased as the number of applied potential cycles was increased, indicating that the starch molecules were subjected to irreversible oxidation reactions that reduced their capacity of storing ionic charges. The capacitance as function of the number of cycles is presented in Fig. 9b. The SLi+G formulation suffered the more pronounced decrease, although it still displayed the highest capacitance levels after 75 cycles. In contrast, the capacitance of the sequential film formulations (where Li salt was added after S was gelatinized), i.e., SG+Li and S+GLi, showed a slight increase during the first 10 cycles, until achieving a stable value after 25–30 cycles. It seems that the application of an exogenous potential reshaped the distribution of the Li salt in the film microstructure, which in turn led to a slight improvement of the electrical capacitance.

Discussion

The results described above showed that the order of addition of components plays an important role in defining the optical, mechanical, and electrical properties of starch-based solid polymer electrolytes. The film microstructure is an important determinant of the characteristics of a solid polymer electrolyte since mobility of ions is favored by amorphous structures [19–21]. It is apparent that re-crystallization mechanism of dispersed starch molecules can be modulated by the order of addition of the lithium salt. Figure 10a shows the existence of an inverse linear correlation ($R^2 = 0.82$) between the conductivity at room temperature and the FTIR ratio $R_{992/1020}$. Also, Fig. 10b shows a similar correlation ($R^2 = 0.97$) between conductivity and enthalpy from DSC analysis. Both the ratio $R_{995/1020}$ and the DSC enthalpy are indicative of short-range crystallinity and ordering in the solid film. In this way, better conductivity values were obtained for films with high content of amorphous structures, which on turn were obtained when the lithium salt was incorporated simultaneously with the native starch granules and the dispersion was gelatinized. Similar behavior was obtained for the electrical capacitance,

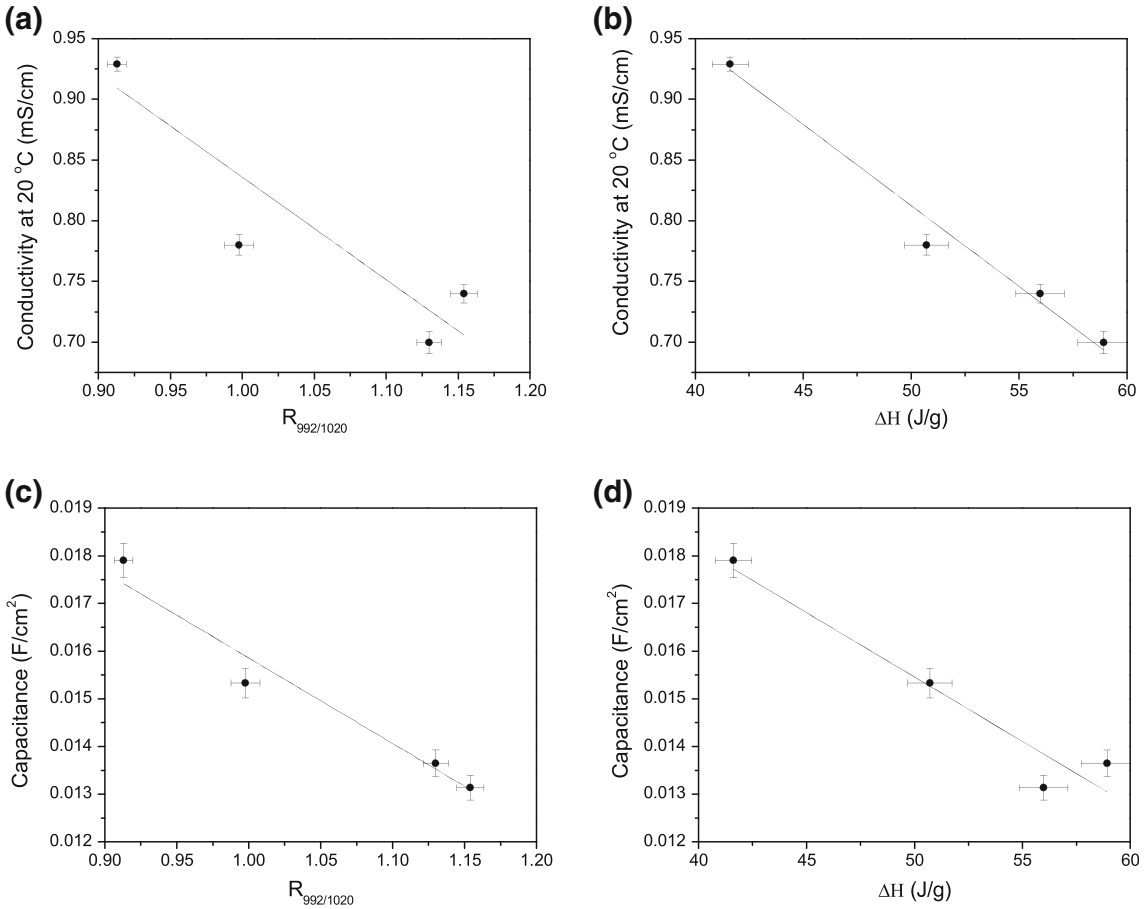

Fig. 10 **a** Inverse linear correlation ($R^2 = 0.82$) between the conductivity at room temperature and the FTIR ratio $R_{992/1020}$. **b** Correlation ($R^2 = 0.97$) between electrical conductivity and enthalpy from DSC analysis. **c** Linear correlation ($R^2 = 0.82$) between the capacitance at room temperature and the FTIR ratio $R_{992/1020}$. **d** Correlation ($R^2 = 0.97$) between electrical capacitance and enthalpy from DSC analysis

as shown by Fig. 10c, d. Inverse linear trends between the FTIR ratio $R_{992/1020}$ and electrical capacitance ($R^2 = 0.94$) and between the DSC enthalpy and the electrical capacitance ($R^2 = 0.88$) were obtained.

On the other hand, the XPS results revealed a possible link between electrical capacitance and the carbon and oxygen ratios $R_{285/286.5}$ and $R_{532.2/532.8}$. In fact, Fig. 11a shows a negative trend between $R_{285/286.5}$ and electrical capacitance of the different film formulations. Recall that the ratio $R_{285/286.5}$ reflects the contribution of carbon atoms bound to carbon or hydrogen atoms relative to carbon atoms bound to oxygen. The decrease of the electrical capacitance with the reduction of $R_{285/286.5}$ suggests that Li ions are likely bonded to hydroxyl groups via, e.g., van der Waals bonds. Figure 9b shows a positive trend between the ratio $R_{532.2/532.8}$ and electrical capacitance, an effect that is related to trend shown in Fig. 11a. In fact, increased values of $R_{532.2/532.8}$ indicate the dominance of carbonyl groups over alcohol groups. It is noted that alcohol groups are introduced by glycerol, so its reduction indicates the interaction of glycerol with starch chains to produce a plasticizing effect.

The mechanisms involved in the variation of electrical properties with the order of addition are not clear at all. It seems that the re-crystallization of starch chains (mainly amylose) could be behind of the phenomenon. Some insights can be obtained from Oosten's theory [28]. Following this theory, starch chains act as a weak acid ion exchanger capable of exchanging starch alcoholic group protons for Li cations from the lithium salt. The Donnan potential established by the negatively charged starch molecules and the positive charge of water prevents the penetration of anions into the molecular structure of starch chains. In turn, the concentration gradient of lithium salt tends to push the Li cations into the starch molecules with the concomitant replacement of hydrogen ions [28]. In this way, the hydrogen ions move to the aqueous phase to achieve a new equilibrium. The binding of Li cations to the starch molecules reduces the instability of dispersed amylose chains and hence the extent of the re-crystallization process. The results in Fig. 8 indicate that the gelatinization process incorporating simultaneously the lithium salt led to a better bonding of the Li cations with respect to the sequential strategy. In the latter case, it is apparent that the distribution of

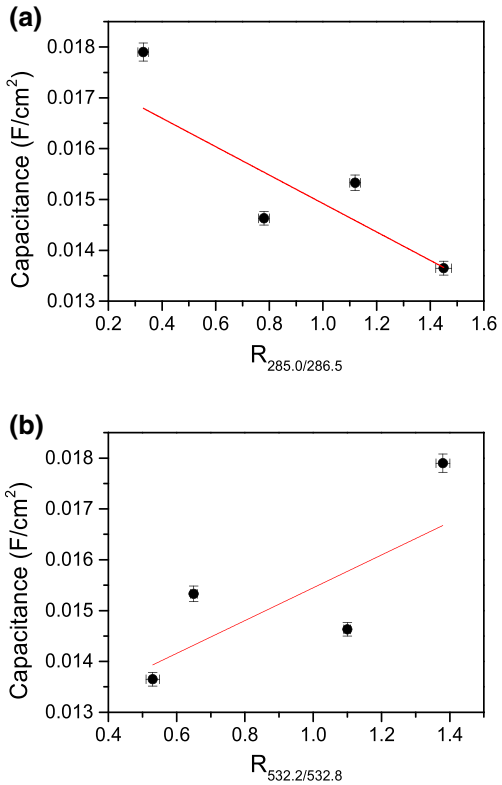

Fig. 11 **a** Inverse relationship ($R^2 = 0.62$) between electrical capacitance and the XPS ratio $R_{285/286.5}$ of the carbon band. **b** Direct relationship ($R^2 = 0.59$) between electrical capacitance and the XPS ratio $R_{532.2/532.8}$ of the carbon band

Li cations is not homogeneous over the gel microstructure with some patches trapped into glycerol domains.

Beyond the particular system considered in this study, the results described above indicate that starch-based solid electrolytes with optimal electrical properties are obtained when the lithium cations are evenly bound into the starch chains dispersed in the gel bulk.

Conclusions

The main conclusion of this study is that the order of addition of the lithium salt and glycerol impacts the properties of electrolytic films. In general, when a starch with added Li salt dispersion is gelatinized (simultaneous formulations), films display weaker mechanical response but improved electrical properties with respect to the sequential addition strategy where the lithium salt is added after the starch gelatinization process. In fact, electrical conductivity and capacitance differences can be higher than 50%. FTIR and DSC analyses suggested that the variations in electrical properties for the different solid electrolyte formulations could be attributed to re-crystallization of starch molecules occurring in the casting phase. It was postulated that Li cation ion replace hydrogen ions inside starch molecules, retarding the re-crystallization of starch molecules. The results of this work should be seen as a guideline towards the design of starch-based solid polymer electrolytes exhibiting optimal electrical properties.

Acknowledgements The authors thank the Consejo Nacional de Ciencia y Tecnología (CONACyT) for partially financing this work through project 236500.

Author's contribution E. J. Vernon-Carter proposed the use of contact angle and EIS for monitoring film stability. J. Alvarez-Ramirez organized results and discussion. L.A. Bello-Perez helped with the characterization of starch-based films. C. Roldan-Cruz (Ph.D. student) designed and performed the EIS experiments. A. Garcia-Hernandez (Ph.D. student) carried out conductivity, opacity, and mechanical response tests. L. Huerta carried out and interpreted XPS studies. All authors contributed to the writing of the manuscript.

Compliance with ethical standards

Conflict of interest The authors declare no competing financial interest.

References

1. Croce F, Appetecchi GB, Persi L, Scrosati B (1998) Nanocomposite polymer electrolytes for lithium batteries. Nature 394:456–458
2. Wu JH, Lan Z, Lin JM, Huang ML, Hao SC, Sato T, Yin S (2007) A novel thermosetting gel electrolyte for stable quasi-solid-state dye-sensitized solar cells. Adv Mater 19:4006–4011
3. Meng C, Liu C, Chen L, Hu C, Fan S (2010) Highly flexible and all-solid-state paperlike polymer supercapacitors. Nano Lett 10(10): 4025–4031
4. Khiar AA, Arof AK (2010) Conductivity studies of starch-based polymer electrolytes. Ionics 16:123–129
5. Khiar ASA, Puteh R, Arof AK (2006) Conductivity studies of a chitosan-based polymer electrolyte. Physica B 373:23–27
6. Yamazaki A, Takegawa R, Kaneko Y, Kadokawa JI, Yamagata M, Ishikawa M (2009) An acidic cellulose–chitin hybrid gel as novel electrolyte for an electric double layer capacitor. Electrochem Commun 11:68–70
7. Park SJ, Yoo K, Kim JY, Kim JY, Lee DK, Kim B, Ko MJ (2013) Water-based thixotropic polymer gel electrolyte for dye-sensitized solar cells. ACS Nano 7:4050–4056
8. Vieira DF, Avellaneda CO, Pawlicka A (2007) Conductivity study of a gelatin-based polymer electrolyte. Electrochim Acta 53:1404–1408
9. Zobel HF (1988) Molecules to granules: a comprehensive starch review. Starch-Stärke 40:44–50
10. Marcondes RF, D'Agostini PS, Ferreira J, Girotto EM, Pawlicka A, Dragunski DC (2010) Amylopectin-rich starch plasticized with glycerol for polymer electrolyte application. Solid State Ionics 181:586–591
11. Sudhakar YN, Selvakumar M (2012) Lithium perchlorate doped plasticized chitosan and starch blend as biodegradable polymer electrolyte for supercapacitors. Electrochim Acta 78:398–405
12. Sudhakar YN, Selvakumar M (2013) $LiClO_4$-doped plasticized chitosan and poly (ethylene glycol) blend as biodegradable polymer electrolyte for supercapacitors. Ionics 19:277–285
13. Kumar M, Tiwari T, Srivastava N (2012) Electrical transport behaviour of bio-polymer electrolyte system: potato starch+ammonium iodide. Carbohydr Polym 88:54–60

14. Lin Y, Li J, Liu K, Liu Y, Liu J, Wang X (2016) Unique starch polymer electrolyte for high capacity all-solid-state lithium sulfur battery. Green Chem 18:3796–3803
15. Biliaderis CG, Maurice TJ, Vose JR (1980) Starch gelatinization phenomena studied by differential scanning calorimetry. J Food Sci 45(6):1669–1674
16. Ratnayake WS, Jackson DS (2007) A new insight into the gelatinization process of native starches. Carbohydr Polym 67:511–529
17. Ning W, Xingxiang Z, Haihui L, Benqiao H (2009) 1-Allyl-3-methylimidazolium chloride plasticized-corn starch as solid biopolymer electrolytes. Carbohydr Polym 76:482–484
18. Ramesh S, Liew CW, Arof AK (2011) Ion conducting corn starch biopolymer electrolytes doped with ionic liquid 1-butyl-3-methylimidazolium hexafluorophosphate. J Non-Cryst Solids 357(21):3654–3660
19. Khanmirzaei MH, Ramesh S (2014) Nanocomposite polymer electrolyte based on rice starch/ionic liquid/TiO_2 nanoparticles for solar cell application. Measurement 58:68–72
20. Wang S, Li C, Copeland L, Niu Q, Wang S (2015) Starch retrogradation: a comprehensive review. Compr Rev Food Sci Food Saf 14: 568–585
21. Li G, Li Z, Zhang P, Zhang H, Wu Y (2008) Research on a gel polymer electrolyte for Li-ion batteries. Pure Appl Chem 80:2553–2563
22. ASTM D1003-00 (2000) Standard test method for haze and luminous transmittance of transparent plastics. ASTM International, West Conshohocken
23. ASTM D882-00 (2000) Standard test method for tensile properties of thin plastic sheeting. ASTM International, West Conshohocken
24. Hermans PH, Weidinger A (1949) X-ray studies on the crystallinity of cellulose. J Polym Sci 4:135–144
25. Ahvenainen P, Kontro I, Svedström K (2016) Comparison of sample crystallinity determination methods by X-ray diffraction for challenging cellulose I materials. Cellulose 23:1073–1086
26. Roldan-Cruz C, Garcia-Hernandez A, Vernon-Carter EJ, Alvarez-Ramirez J (2017) Impact of insoluble starch remnants on the behavior of corn starch/glycerol/LiCl solid electrolyte. Ionics. doi:10.1007/s11581-017-2014-0
27. Romero-Bastida CA, Bello-Perez LA, Velazquez G, Alvarez-Ramirez J (2015) Effect of the addition order and amylose content on mechanical, barrier and structural properties of films made with starch and montmorillonite. Carbohydr Polym 127:195–201
28. Oosten BJ (1982) Tentative hypothesis to explain how electrolytes affect the gelatinization temperature of starches in water. Starch-Stärke 34:233–239
29. Lobato-Calleros C, Hernandez-Jaimes C, Chavez-Esquivel G, Meraz M, Sosa E, Lara VH, Alvarez-Ramirez J, Vernon-Carter EJ (2015) Effect of lime concentration on gelatinized maize starch dispersions properties. Food Chem 172:353–360
30. Xian-Zhong H, Hamaker BR (2002) Association of starch granule proteins with starch ghosts and remnants revealed by confocal laser scanning microscopy. Cereal Chem 79:892–896
31. Debet MR, Gidley MJ (2007) Why do gelatinized starch granules not dissolve completely? Roles for amylose, protein, and lipid in granule "ghost" integrity. J Agric Food Chem 55:4752–4760
32. Ma X, Yu J, He K, Wang N (2007) The effects of different plasticizers on the properties of thermoplastic starch as solid polymer electrolytes. Macromol Mat Eng 292:503–510
33. Liew CW, Ramesh S, Ramesh K, Arof AK (2012) Preparation and characterization of lithium ion conducting ionic liquid-based biodegradable corn starch polymer electrolytes. J Solid State Electrochem 16:1869–1875
34. Utrilla-Coello RG, Hernández-Jaimes C, Carrillo-Navas H, González F, Rodríguez E, Bello-Perez LA, Alvarez-Ramirez J (2014) Acid hydrolysis of native corn starch: morphology, crystallinity, rheological and thermal properties. Carbohydr Polym 103: 596–602
35. Karim AA, Norziah MH, Seow CC (2000) Methods for the study of starch retrogradation. Food Chem 71:9–36
36. Sevenou O, Hill SE, Farhat IA, Mitchell JR (2002) Organisation of the external region of the starch granule as determined by infrared spectroscopy. Int J Biol Macromol 31(1):79–85
37. van Soest JJ, Tournois H, de Wit D, Vliegenthart JF (1995) Short-range structure in (partially) crystalline potato starch determined with attenuated total reflectance Fourier-transform IR spectroscopy. Carbohydr Res 279:201–214
38. Beck M, Jekle M, Becker T (2011) Starch re-crystallization kinetics as a function of various cations. Starch-Stärke 63:792–800
39. Al-Muhtaseb AH, McMinn WAM, Magee TRA (2004) Water sorption isotherms of starch powders. Part 2: thermodynamic characteristics. J Food Eng 62:135–142
40. Liu H, Chaudhary D, Yusa S, Tadé MO (2011) Glycerol/starch/Na^+-montmorillonite nanocomposites: a XRD, FTIR, DSC and ^1H NMR study. Carbohydr Polym 83:1591–1597
41. Talja RA, Helén H, Roos YH, Jouppila K (2007) Effect of various polyols and polyol contents on physical and mechanical properties of potato starch-based films. Carbohydr Polym 67:288–295
42. Huang X, Kocaefe D, Kocaefe Y, Boluk Y, Pichette A (2012) Study of the degradation behavior of heat-treated jack pine (*Pinus banksiana*) under artificial sunlight irradiation. Polym Degrad Stab 97:1197–1214
43. Samsudin AS, Khairul WM, Isa MIN (2012) Characterization on the potential of carboxy methylcellulose for application as proton conducting biopolymer electrolytes. J Non-Cryst Solids 358:1104–1112
44. Shukur MF, Kadir MFZ (2015) Hydrogen ion conducting starch-chitosan blend based electrolyte for application in electrochemical devices. Electrochim Acta 158:152–165
45. Selvakumar M, Bhat DK (2008) $LiClO_4$ doped cellulose acetate as biodegradable polymer electrolyte for supercapacitors. J Appl Polym Sci 110:594–602
46. Stephan AM, Thirunakaran RN, Renganathan G, Sundaram V, Pitchumani S, Muniyandi N, Ramamoorthy P (1999) A study on polymer blend electrolyte based on PVC/PMMA with lithium salt. J Power Sources 81:752–758
47. Jaipal Reddy M, Sreekanth T, Subba Rao UV (1999) Study of the plasticizer effect on a (PEO+$NaYF_4$) polymer electrolyte and its use in an electrochemical cell. Solid State Ionics 126:55–63
48. Teoh KH, Lim CS, Ramesh S (2014) Lithium ion conduction in corn starch based solid polymer electrolytes. Measurement 48:87–95